RESEARCH ARTICLE

PROGRESS IN
PHOTOVOLTAICS WILEY

Silicon solar cell–integrated stress and temperature sensors for photovoltaic modules

Andreas J. Beinert[1,2] 🆔 | Mark Imm[1,3] | Jan Benick[1] | Felix Becker[3] |
Sonja Seitz[1] | Martin Heinrich[1] | Oliver Paul[3] | Stefan W. Glunz[1,4] |
Jarir Aktaa[2] | Ulrich Eitner[1] | Holger Neuhaus[1]

[1]Module Technology Department, Fraunhofer Institute for Solar Energy Systems ISE, Freiburg, Germany

[2]Institute for Applied Materials, Karlsruhe Institute of Technology (KIT), Eggenstein-Leopoldshafen, Germany

[3]Department of Microsystems Engineering (IMTEK), University of Freiburg, Freiburg, Germany

[4]Department of Sustainable Systems Engineering (INATECH), University of Freiburg, Freiburg, Germany

Correspondence
Andreas J. Beinert, Module Technology Department, Fraunhofer Institute for Solar Energy Systems ISE, Heidenhofstrasse 2, Freiburg 79110, Germany.
Email: Andreas.Beinert@ise.fraunhofer.de

Funding information
Cusanuswerk

Abstract

We propose silicon solar cell–integrated stress and temperature sensors as a new approach for the stress and temperature measurement in photovoltaic (PV) modules. The solar cell–integrated sensors enable a direct and continuous in situ measurement of mechanical stress and temperature of solar cells within PV modules. In this work, we present a proof of concept for stress and temperature sensors on a silicon solar cell wafer. Both sensors were tested in a conventional PV module setup. For the stress sensor, a sensitivity of $(-47.41 \pm 0.14)\%/\text{GPa}$ has been reached, and for the temperature sensor, a sensitivity of $(3.557 \pm 0.008) \times 10^{-3}\ \text{K}^{-1}$ has been reached. These sensors can already be used in research for increased measurement accuracy of the temperature and the mechanical stress in PV modules because of the implementation at the precise location of the solar cells within a laminate stack, for process evaluation, in-situ measurements in reliability tests, and the correlation with real exposure to climates.

KEYWORDS

in situ measurement, predictive maintenance, PV module, stress measurement, stress sensor, temperature measurement, temperature sensor

1 | INTRODUCTION

Degradation of photovoltaic (PV) modules in the field still leads to a significant power loss of PV systems.[1-4] Moreover, the detection of degradation is often related to elaborate and time-consuming characterization methods. Among them are visual inspection, current-voltage (IV) curve analysis, electroluminescence imaging, thermography, and ultraviolet (UV) fluorescence.[2] However, they all detect the degradation effect, not the stress origin. There are also a few methods known for a predictive failure analysis, eg, using thermography in combination with smart algorithms[5] or maximum power point tracking

(MPPT).[6] However, the thermography is not capable for a continuous analysis, and the MPPT only detects failures when they occur.

We propose a different and novel approach for predictive maintenance analysis: sensors that are integrated into the solar cell itself. The advantage of solar cell–integrated sensors is the possibility of continuous in situ measurements on cell level. In this work, we present first results of stress and temperature sensors, which are integrated into silicon solar cell wafers and hence measure the stress and temperature of the solar cell wafer itself. The presented sensors have the purpose to be used in research and development, for example, in mechanical load or thermal cycling tests according to the test norm

IEC 61215.[7] They can help in obtaining a deeper understanding of the module technology and investigate the influence of new solar cell or module concepts on it. Possible applications are the development of lightweight PV modules or the heating of solar cells by reverse operation. Further research will focus on transferring the sensors to functional solar cells and a use in conventional PV modules.

Each sensor covers only a small part of the solar cell; hence, the interaction with the solar cell and the PV module is minimized, which is the requirement for a reasonable in situ measurement. Both sensors can be manufactured by using processes typically applied in the solar cell production. Hence, they can be applied to all silicon-based solar cells, either on the front or back side. Also, existing solar cell production lines could be modified for the sensor implementation.

In this work, the basic principles, manufacturing methods, and sensitivity measurements of different sensor designs are described. The sensors have been manufactured on silicon solar cell wafers with lab-scale silicon solar cell production processes and are integrated into a module setup. Section 2 describes the stress sensor, and Section 3 the temperature sensor. Section 4 gives an overall conclusion.

2 | STRESS SENSOR

Cell cracks induced by tensile stress[8,9] can account for PV module degradation rates of up to 8% relative power loss per year.[1] Recently (synchrotron) X-ray[10,11] and Raman microdiffraction[12,13] were presented as methods to measure the stress in solar cells encapsulated in a PV module. Both methods are capable of measuring the residual stress in solar cells. However, since they are based on the interaction of light with solar cells, the measurement has to be performed with a special setup and usually in a laboratory. Consequently, in situ measurements are very challenging for these methods. Another optical method used previously is the measurement of the cell gap displacement by digital image correlation.[14] Since this is also an optical method, the same restrictions apply. A nonoptical method would be the use of foil strain gauges, which have several disadvantages. For example, the foil strain gauge is adhered to the encapsulant and the solar cell; therefore, the strain in the gauge cannot be assigned to one layer. In addition, inserting the foil strain gauge into the laminate modifies its thermomechanical properties.

To overcome these issues, we have developed a piezoresistive stress sensor, which is integrated into the silicon solar cell wafer. Therefore, it measures the stress in the solar cell itself without interfering with it. The sensor is based on the piezoresistive effect of silicon, which is well-known and used for sensor applications in the field of microelectronics.[15-18] We transfer the method to p-type monocrystalline silicon solar cell wafers and use lab-scale silicon solar cell production technologies. The stress sensor is realized as a rectangular piezoresistive resistor using high local n-doping by ion implantation, as depicted in Figure 1, and subsequent silver metallization. To shield the sensor from the electrons generated in the adjacent silicon, a highly p-doped shielding guard ring (set to ground in the characterization measurements) is implemented around the sensor.
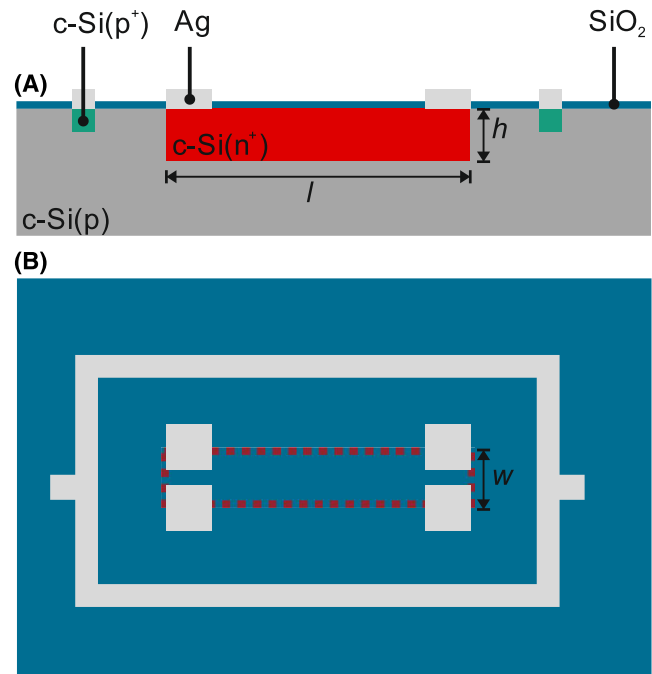

FIGURE 1 Schematic drawing of the piezoresistive stress sensor. (A) Cross-sectional view: the sensor consists of a highly n-doped area within the p-doped substrate and a highly p-doped shielding ring. Both are contacted by Ag metallization. (B) Top view: the p-doped area of the shielding is hidden by the metallization. The dotted line indicates the shape of the piezoresistive sensor part, which is hidden by the SiO₂ layer, not to scale [Colour figure can be viewed at wileyonlinelibrary.com]

2.1 | Theory

The sensor resistance $R_{\sigma,0}$ depends on the sheet resistance $R_{\square}$ of the n-doped layer, its length l, and width w:

$$R_{\sigma,0} = R_{\square}\frac{l}{w}. \tag{1}$$

If an external stress is applied to the sensor, the change of resistance ΔR_{σ} can be expressed in first-order approximation by the piezoresistive tensor $\boldsymbol{\pi}$, which also reflects the anisotropy of silicon.[17] Note that tensors are printed in bold.

$$\Delta\vec{R}_{\sigma} = R_{\sigma,0}\,\boldsymbol{\pi}\,\vec{\sigma}, \tag{2}$$

with $\vec{\sigma}$ being the stress vector in the so-called Voigt notation, which transfers the symmetric 3 × 3 stress tensor to a six-dimensional vector.

For a uniaxial stress, which is the case for a 4-point bending test, the stress vector $\vec{\sigma}$ has just one component σ_{xx}, and Equation (2) reduces to

$$\Delta R_{\sigma} = R_{\sigma,0}\,\pi_{11}\sigma_{xx}. \tag{3}$$

The piezoresistive coefficient π_{11} depends on the temperature T and the charge carrier concentration N, which can be described using the dimensionless factor P.[19]

$$\pi_{11}(T,N) = \pi_{11,ref}\,P(T,N), \tag{4}$$

where $\pi_{11,ref}$ is the piezoresistive coefficient at room temperature and a given charge carrier concentration N_{ref}. With Equations (1) and (4), the change in resistance ΔR_σ because of a uniaxial stress becomes

$$\Delta R_\sigma = R_\square \frac{l}{w} \pi_{11,ref} P(T,N) \sigma_{xx}. \tag{5}$$

Hence, in addition to stress, the resistance change ΔR_σ is influenced by the sheet resistance $R_\square$, the aspect ratio $a = l/w$, the charge carrier concentration N, and the temperature T. The latter dependence vanishes for sufficiently high charge carrier concentrations ($\gg 10^{20}$ cm^{-3}).[19]

2.2 | Method

In this work, we use a target sheet resistance $R_\square$ of 100 Ω/sq and vary the aspect ratio a and the charge carrier concentration N. Table 1 shows the chosen design variations.

The sensors were produced at the Fraunhofer Institute for Solar Energy Systems ISE on p-type float zone silicon solar wafers with a specific resistance of 1 Ωcm and a thickness of 250 μm. On each wafer, 40 sensors were placed in a way that the wafer can be cut into stripes containing four sensors (see Section 2.2.1).

Figure 2 shows the process flow with the relevant process parameters. The first process step is the boron implantation for the shield

TABLE 1 Design variations of the piezoresistive stress sensor

Variation	Charge Carrier Concentration N, cm^{-3}	Aspect ratio a, —	Resistance R_σ, Ω
S.1	1×10^{19}	5	500
S.2	1×10^{19}	10	1000
S.3	1×10^{19}	50	5000
S.4	5×10^{19}	5	500
S.5	5×10^{19}	10	1000
S.6	5×10^{19}	50	5000

guard ring. A boron dose of 5×10^{15} cm^{-2} is used with an annealing at 1050 °C (80 minutes, O$_2$ atmosphere). In the second step, the phosphorous implantation takes place. We use two different doses: (a) 5.25×10^{14} cm^{-2} with an annealing at 1050 °C (80 minutes, O$_2$ atmosphere), labeled N^+, and (b) 9×10^{14} cm^{-2} with an annealing time of 30 minutes at 950 °C (Ar atmosphere), labeled N^{++}. In the last step, metal is evaporated (e-gun). The metallization consists of a stack of titanium, palladium, and silver with layer thicknesses of 50, 50, and 1000 nm, respectively. For all structures, a positive photoresist was used in photolithography. All implantations as well as the evaporation were done on a beamline implanter (*VIISta HC, Applied Materials*). For annealing, a *centrotherm* tube furnace *E1550 HT 300-4* was used.
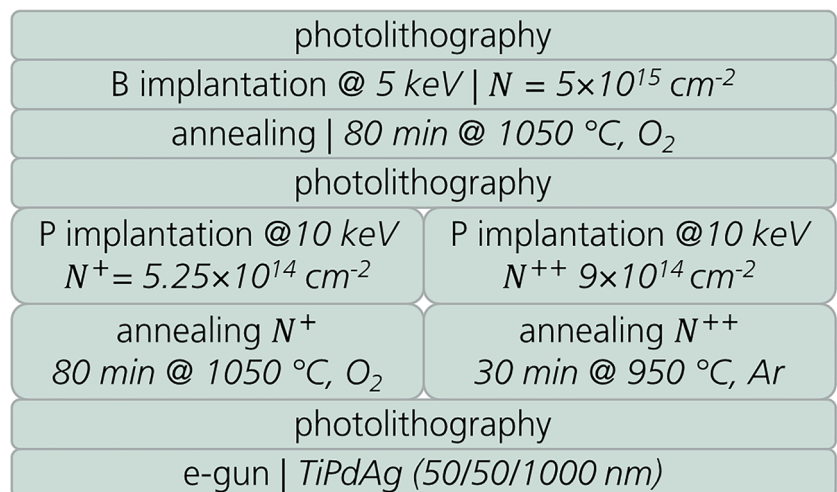
The doping profiles were analyzed using electrochemical capacitance-voltage (ECV) measurements, shown in Figure 3. For the N^+-profile, a charge carrier surface concentration of 1×10^{19} cm^{-3} was measured, and for the N^{++}-profile, a surface concentration of 5×10^{19} cm^{-3} was measured.

2.2.1 | Characterization

For the characterization on a 4-point bending bridge,[20] we split the wafers into single stripes of 10×100 mm^2 using a laser. Each stripe contains four different sensor variations. The current was measured for two sensors at a time. The distance of the 4-point bending supports were set so that both sensors are exposed to the same stress. In pretests, we found that the sensor stripes fracture at around 90 MPa; therefore, we limit the test range to 65 MPa and subdivide it into 13 load steps. At each load step, the current at an applied voltage of 1 V is measured by an electrical 4-point probe. From the data, we calculate the change of resistance ΔR_σ relative to 0 MPa. We then plot the relative resistance change $\Delta R_\sigma / R_{\sigma,0}$ over the uniaxial stress σ_{xx} (see Figure 4). Finally, we evaluate the sensitivity S_σ of the sensor by performing a linear fit with

$$S_\sigma = \frac{\Delta R_\sigma}{R_{\sigma,0} \Delta \sigma_{xx}}. \tag{6}$$

FIGURE 2 Process flow of stress sensor fabrication. P: phosphorus; B: boron; e-gun: electron beam physical vapor deposition; TiPdAg: titanium, palladium, and silver [Colour figure can be viewed at wileyonlinelibrary.com]
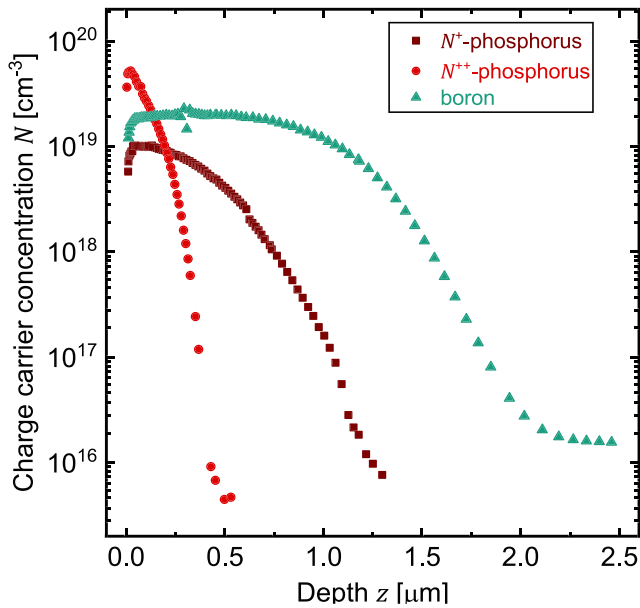

> photolithography
> B implantation @ *5 keV* | *N = 5×10^{15} cm^{-2}*
> annealing | *80 min @ 1050 °C, O$_2$*
> photolithography
> P implantation @*10 keV* N^+= *5.25×10^{14} cm^{-2}* | P implantation @*10 keV* N^{++} *9×10^{14} cm^{-2}*
> annealing N^+ *80 min @ 1050 °C, O$_2$* | annealing N^{++} *30 min @ 950 °C, Ar*
> photolithography
> e-gun | *TiPdAg (50/50/1000 nm)*

FIGURE 3 Measured doping profiles of the N^+ (dark red) and N^{++} (red) profile of the piezoresistor and the boron profile of the shield guard ring (green) [Colour figure can be viewed at wileyonlinelibrary.com]

We have characterized between 10 and 19 sensors of each design variation.

2.3 | Results and discussion

Figure 4 exemplarily shows the relative resistance change of one sensor type from variation S.5. As expected from Equation (5), the resistance shows a linear dependency on the applied stress.

Figure 5 shows the sensitivities of all six design variations as a box plot diagram. The sensitivity decreases with increasing aspect ratio a as well as with increasing charge carrier concentration N. From the equations above, the sensitivity S_σ should be independent of both factors. We assume that the dependency originates from neglecting higher order terms in the equations above, which can be found in Doll and Pruit.[21]

Design variation S.5 (a = 10/1, N = 5×10^{19} cm^{-3}) has the smallest deviation; therefore, we choose to further investigate this design. It has a sensitivity of (-47.41 ± 0.14)%/GPa.

2.3.1 | Module integration

We laminate the chosen sensor design S.5 using a conventional PV module setup (Figure 6), with a 14.7×10.5-cm^2 and 1-mm thin glass, EVA, and a TPT backsheet.

We use a 3-point bending setup to measure the resistance R_σ during bending to failure. Using the above sensitivity, we convert the resistance change ΔR_σ to stress. We have obtained a linear correlation between the deflection and the relative change in resistance. The
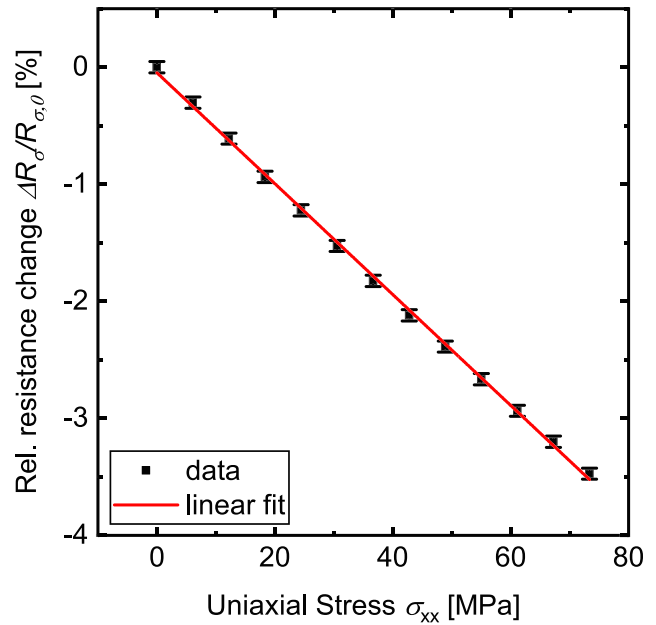

FIGURE 4 Relative resistance change vs uniaxial stress for one exemplary sensor from variation S.5. The solid red line is a linear fit to the data from which the sensitivity S_σ is obtained [Colour figure can be viewed at wileyonlinelibrary.com]
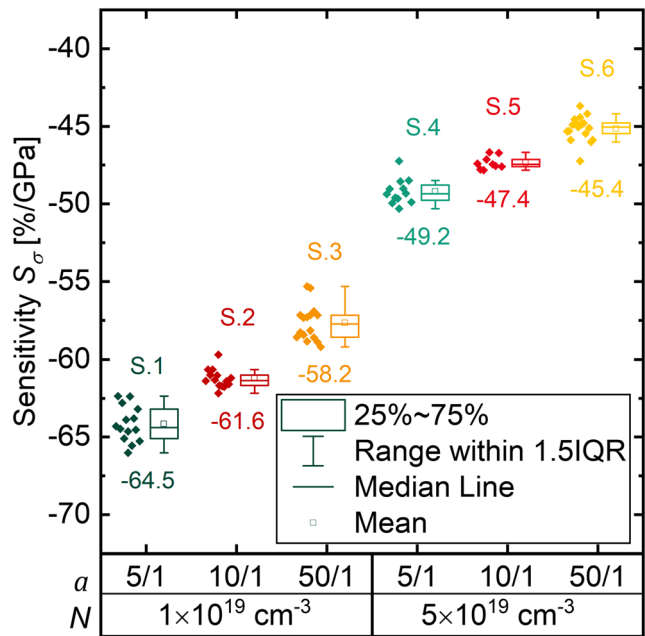

FIGURE 5 Sensitivity of the six different stress sensor variations. On the x-axis are the aspect ratio a and the charge carrier concentration N . The box is the interquartile range (IQR), ie, the range in which the middle 50% of the data lie, the line within the box is the median, and the square is the mean; the whiskers show the range in which 1.5IQR of the data lie [Colour figure can be viewed at wileyonlinelibrary.com]

interconversion into stress reveals that the silicon stripe is in compressive stress, which is shown in Figure 7. The step at around 0.6-mm deflection originates from a small fracture of the solder joint, the
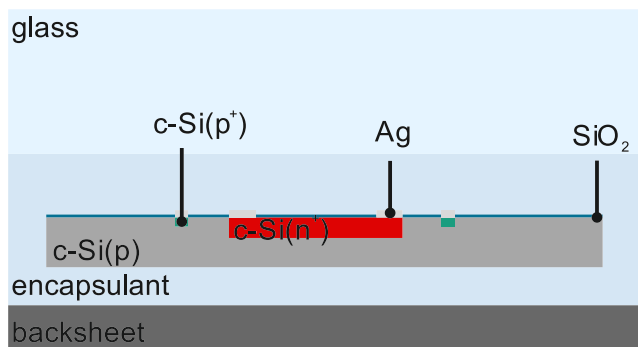
FIGURE 6 Setup of the laminated sensor stripe. A standard glass-foil setup is used with EVA as encapsulant and a 1-mm thin glass, not to scale [Colour figure can be viewed at wileyonlinelibrary.com]
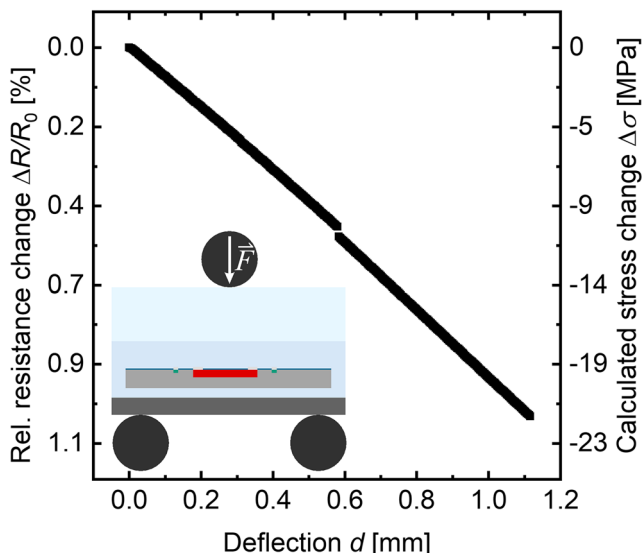

FIGURE 7 Stress measured in a laminated sensor stripe in 3-point bending. The stress change is calculated from the relative resistance change $\Delta R_\sigma / R_{\sigma,0}$ using a sensitivity S_σ of -47.41%/GPa. The insert shows the 3-point bending setup schematically; please note that the left axis is reversed [Colour figure can be viewed at wileyonlinelibrary.com]

metallization, the glass, or the silicon stripe, which does not affect the sensors performance, but induces a sudden change of the measured resistance and hence the calculated stress. However, the stress value change is only 0.5 MPa and therefore is not significant. The successful measurement of bending stress proves that the proposed sensor is capable to determine stress within a PV module setup.

3 | TEMPERATURE SENSOR

The PV modules temperature influences not only the reliability but also its performance.[22] Accordingly, several methods were proposed to determine the PV module temperature in the past. The most common method is the use of temperature sensors such as thermocouples,[22-24] which are either laminated into or attached to the rear side of the PV module. The former has the disadvantage that the PV module setup is modified by the sensor, and because of its height, the temperature cannot be assigned to one layer. The latter does not allow an accurate temperature measurement within the PV module.[24] Another approach is infrared (IR) imaging,[23] which is capable of resolving the temperature of solar cells. However, IR imaging for permanent measurements during operation and testing is rather costly and therefore applied occasionally, only. Also, the silicon solar cell itself is used as a temperature sensing device by utilizing the temperature dependency of the voltage.[23] However, since the voltage depends on various factors, the operation conditions, especially the irradiation, need to be determined as well.

We present a temperature sensor, which can be integrated into the silicon solar cell itself. Hence, it can measure the solar cell temperature directly without interfering with the PV module setup. Figure 8 shows a schematic drawing of the proposed design.

3.1 | Theory and method

We utilize the temperature sensitivity of the silver used for metallization and develop a sensor equivalent to a Pt100 sensor. Accordingly, we design a structure with a nominal resistance $R_{T,0}$ at $0°C$ of $100\ \Omega$. The resistance $R_{T,0}$ depends on the specific resistance ρ, length l, width w, and height h:

$$R_{T,0} = \rho \frac{l}{hw}. \qquad (7)$$

The temperature dependence is expressed by the resistance temperature coefficient α_T:
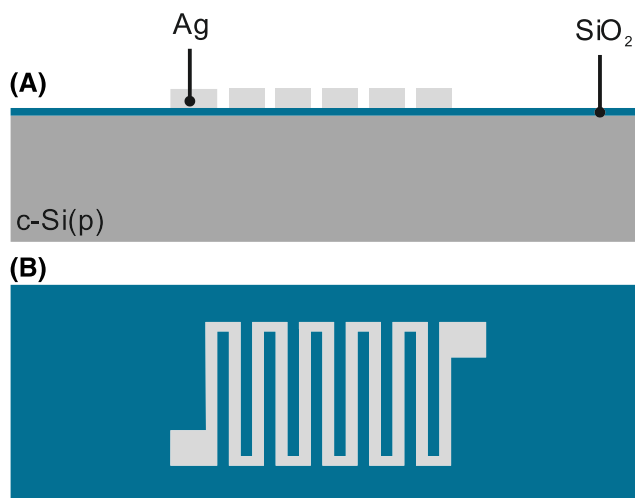

FIGURE 8 Schematic drawing of the resistive temperature sensor. (A) Cross-sectional view with the metallization insulated from the substrate by silicon oxide. (B) Top view with the meander like structure of the metallization, not to scale [Colour figure can be viewed at wileyonlinelibrary.com]

$$R_T(T) = R_{T,0}(1 + \alpha_T\, T), \qquad (8)$$

where $R_{T,0}$ and α_T are defined for 0°C and T denotes temperature in °C.

Because of the relatively low specific resistance ρ of silver of about 1.6×10^{-5} Ωmm,[25] the sensor is designed as a meander to allow a small size while achieving a resistance of 100 Ω. The silicon oxide layer is used as an electrical insulation layer from the sensor cell.

The sensors are manufactured on the same solar cell wafer as the stress sensors (see Section 2.2) at Fraunhofer ISE. We use the same process as for the stress sensor metallization (Figure 9). This technique is commonly used for contact formation of high-efficiency solar cells.

3.1.1 | Characterization

We measure the resistance R_T using an electrical 4-point probe setup during three temperature cycles in the range of −40 ⋯ + 160°C for eight different sensors. The actual temperature is measured with at least two type K thermocouples. In each cycle, we increase the temperature in steps of 10 K with a slope of 2 K/min and hold it for 10 minutes before measurement to have a stable temperature during the measurement. We then plot the measured resistance R_T versus the temperature (see Figure 10) and finally determine the sensitivity S_T, which is the resistance temperature coefficient α_T, by a linear fit:

$$S_T = \alpha_T = \frac{\Delta R_T}{R_{T,0}\, \Delta T}. \qquad (9)$$

We determine the resistance temperature coefficient α_T for each cycle for the heating and cooling phase separately. For each sensor, we draw the mean over all cycles and phases and finally over all eight sensors.

3.2 | Results and discussion

The variance of the eight sensors is not significant. Therefore, exemplarily results of Sensor 1 are shown in Figure 10. The mean resistance temperature coefficient α_T is $(3.557 \pm 0.008)\ 10^{-3}\ \mathrm{K}^{-1}$. The mean value of $R_{T,0}$ is (100.6 ± 0.3) Ω.
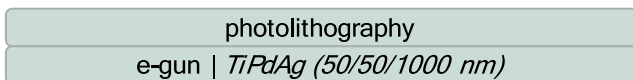
FIGURE 9 Process flow of temperature sensor fabrication. e-gun: electron beam physical vapor deposition; TiPdAg: titanium, palladium, and silver [Colour figure can be viewed at wileyonlinelibrary.com]
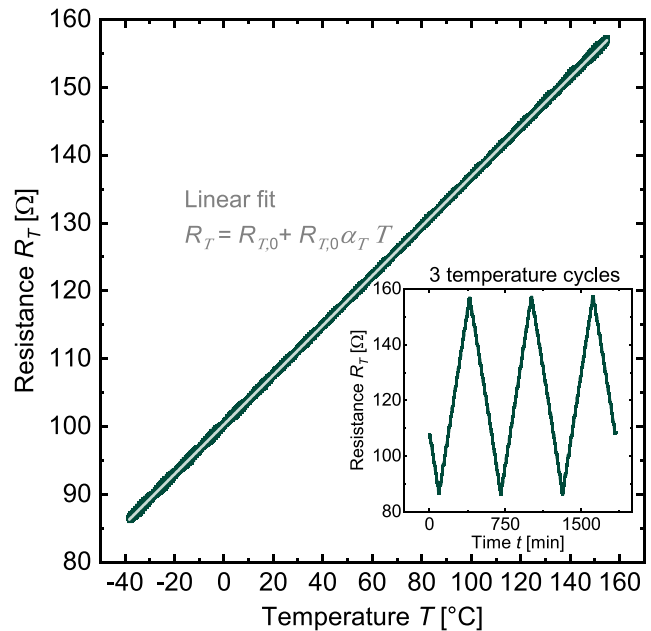
FIGURE 10 Temperature-dependent resistance R_T of one exemplary temperature sensor. The data represents three temperature cycles shown in the insert. The line is a linear fit [Colour figure can be viewed at wileyonlinelibrary.com]

3.3 | Module integration

We laminate one silicon stripe containing three temperature sensors using the above-mentioned standard PV module setup (see Figure 6) with a 20×20-cm² front glass of 3 mm thickness. Next to the sensor
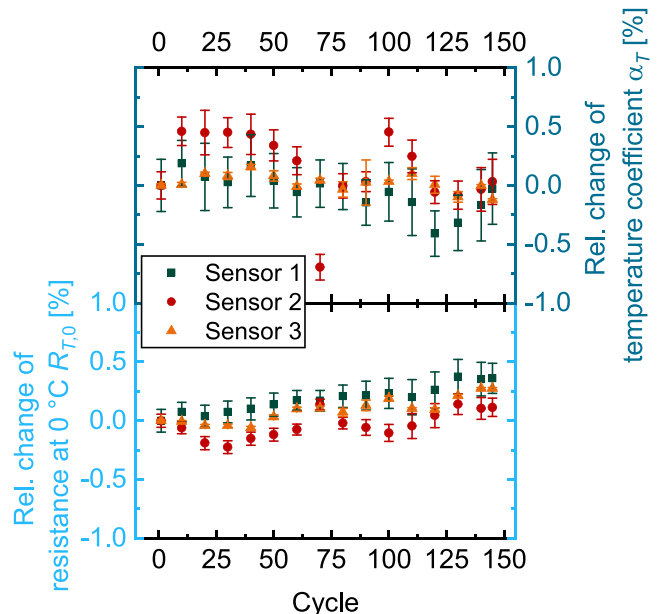
FIGURE 11 Change of 0°C resistance $R_{T,0}$ (bottom) and the resistance temperature coefficient α_T (top) for three module-integrated sensors during 145 thermal cycles. The values are evaluated each 10 cycles; the change is relative to the first cycle [Colour figure can be viewed at wileyonlinelibrary.com]

stripe, we place two type K thermocouples. We then expose the laminated sensor stripe to 145 temperature cycles between -35°C and $+85^\circ$C with a slope of 8.3 K/min and a holding time at the minimum and maximum temperature of 15 minutes. Using a 4-point probe, we measure the resistance each 1.5 minutes. Figure 11 shows the relative change of the 0°C resistance $R_{T,0}$ and of the temperature coefficient α_t each 10th cycle. The results indicate a slight increase of less than 0.5% of the 0°C resistance $R_{T,0}$, most likely due to a slight degradation of the solder joint. However, the temperature coefficient α_t does not show this systematic change. We chose a fairly high-temperature gradient during the thermal cycles to minimize the testing time. Consequently, the variability of the temperature coefficient α_t is up to 0.75%. Since this is still a relatively low value and the temperature gradient occurring in the field is lower, we conclude that the sensors are capable of determining the temperature of silicon solar cells within a PV module.

4 | CONCLUSION

We propose a new approach for predictive maintenance measurements of PV modules: silicon solar cell–integrated sensors. In this work, we present a stress and a temperature sensor, which are integrated in silicon solar cell wafers. The sensors are manufactured using only silicon solar cell production processes and can already be used in research and development.

The stress sensor utilizes the piezoresistive effect of silicon by high local doping. The presented sensors are produced on p-doped float zone solar cell wafers. Accordingly, the sensing part consists of a highly n-doped area. Six different designs with varying aspect ratio a and charge carrier concentration N are compared. All designs resolve the stress in the test specimens and have sensitivities in the range between -45 and -65%/GPa. The lowest scattering is achieved for the design with $a = 10/1$, $N = 5{\times}10^{19}$ cm^{-3}, which has a sensitivity of $(-47.41 \pm 0.14)\%$/GPa. The module integration of this design shows that the sensors are capable of measuring the stress in laminated solar cells.

The temperature sensor utilizes the temperature dependence of the silver metallization. We propose a meander style design with a 0°C resistance of 100 Ω. The produced sensors have a value of (100.6 ± 0.3) Ω with a resistance temperature coefficient α_T, which is the sensitivity of the sensors of (3.557 ± 0.008) 10^{-3} K^{-1}. Laminated sensors show a good stability in 145 temperature cycles from -35°C to $+85^\circ$C. Therefore, we conclude that the proposed sensors are indeed capable of measuring the temperature in laminated silicon solar cells.

The presented sensors can already be applied for research and development purpose, such as monitoring temperature and stress in laminates precisely at the location of solar cells with the methods described above. By using an electrical 4-point probe setup, the influence of the measurement cables leaving the PV module is negligible. In further works, we implement the sensors on electrically functional solar cells. With this, further investigations will be carried out on the following topics: the impact on the solar cells efficiency, long-term stability of the sensors, and the shielding from the solar cell. Since the area covered by the sensors is very small and they can be applied on the back side of the solar cell, we do not expect significant efficiency losses. We also expect good long-term stability because only solar cell production processes are used. These solar cell–integrated sensors will enable an integrated direct and continuous in situ monitoring of the solar cells stress and temperature within a PV module. For an implementation into commercial PV modules, further research is needed, eg, on a wireless data transmission along with a self-powering approach, which we see as the main challenge for an in situ monitoring.

ORCID

Andreas J. Beinert [ID] https://orcid.org/0000-0001-6885-3243

REFERENCES

1. Köntges M, Oreski G, Jahn U, et al. Assessment of photovoltaic module failures in the field. Report IEA-PVPS T13–09:2017; 2017.
2. Köntges M, Altmann S, Heimberg T, Jahn U, Berger KA. Mean degradation rates in PV systems for various kinds of PV module failures. In: Proceedings of the 32nd European Photovoltaic Solar Energy Conference and Exhibition (EU PVSEC); 2016; pp. 1435–1443. https://doi.org/10.4229/EUPVSEC20162016-5DP.1.2.
3. Jordan DC, Kurtz SR, VanSant K, Newmiller J. Compendium of photovoltaic degradation rates. *Progress in Photovoltaics: Research and Applications*. 2016;24(7):978-989. https://doi.org/10.1002/pip.2744
4. Jordan DC, Kurtz SR. Photovoltaic degradation rates—an analytical review. *Progress in Photovoltaics: Research and Applications*. 2013;21(1):12-29. https://doi.org/10.1002/pip.1182
5. Jaffery ZA, Dubey AK, Khan I, Haque A Scheme for predictive fault diagnosis in photo-voltaic modules using thermal imaging *Infrared Physics & Technology* 2017; 83, 182–187. https://doi.org/10.1016/j.infrared.2017.04.015.
6. Roman E, Alonso R, Ibanez P, Elorduizapatarietxe S, Goitia D. Intelligent PV module for grid-connected PV systems. *IEEE Transactions on Industrial Electronics*. 2006;53(4):1066-1073. https://doi.org/10.1109/TIE.2006.878327
7. International Electrotechnical Commission (IEC). Terrestrial photovoltaic (PV) modules—Design qualification and type approval—Part 2: test procedures (IEC 61215-2:2016). Geneva, Switzerland: International Electrotechnical Commission (IEC); 2016.
8. Köntges M, Kunze I, Kajari-Schroeder S, Breitenmoser X, Bjørneklett B. The risk of power loss in crystalline silicon based photovoltaic modules due to micro-cracks. *Sol Energ Mat Sol C*. 2011; 95(4):1131-1137. https://doi.org/10.1016/j.solmat.2010.10.034
9. Kaule F, Wang W, Schönfelder S. Modeling and testing the mechanical strength of solar cells. *Sol Energ Mat Sol C*. 2014;120(Part A):441-447. https://doi.org/10.1016/j.solmat.2013.06.048
10. Handara VA, Radchenko I, Tippabhotla SK, et al. Probing stress and fracture mechanism in encapsulated thin silicon solar cells by synchrotron X-ray microdiffraction. *Sol Energ Mat Sol C*. 2017;162:30-40. https://doi.org/10.1016/j.solmat.2016.12.028

11. Meng X, Stuckelberger M, Ding L, West B, Jeffries A, Bertoni M. Quantitative mapping of deflection and stress on encapsulated silicon solar cells. *IEEE Journal of Photovoltaics*. 2018;8(1):189-195. https://doi.org/10.1109/JPHOTOV.2017.2768959

12. Mühleisen W, Schicker J, Neumaier L, et al. Stress measurements in interconnected solar cells with Raman spectroscopy. In: Proceedings of the 31st European Photovoltaic Solar Energy Conference and Exhibition (EU PVSEC); 2015: 160–163. https://doi.org/10.4229/EUPVSEC20152015-1BV.6.38.

13. Beinert AJ, Büchler A, Romer P, et al. Enabling the measurement of thermomechanical stress in solar cells and PV modules by confocal micro-Raman spectroscopy. *Sol Energ Mat Sol C*. 2019;193:351-360. https://doi.org/10.1016/j.solmat.2019.01.028

14. Eitner U, Köntges M, Brendel R. Use of digital image correlation technique to determine thermomechanical deformations in photovoltaic laminates: measurements and accuracy. *Sol Energ Mat Sol C*. 2010;94(8):1346-1351. https://doi.org/10.1016/j.solmat.2010.03.028

15. Gieschke P, Paul O. CMOS-integrated sensor chip for in-plane and out-of-plane shear stress. *Procedia Engineering*. 2010;5:1364-1367. https://doi.org/10.1016/j.proeng.2010.09.368

16. Gieschke P, Sbierski B, Paul O. CMOS-based piezo-FET stress sensors in Wheatstone bridge configuration. In: Proceedings of the IEEE Sensors 2011; 2011: 93–96, https://doi.org/10.1109/ICSENS.2011.6127299.

17. Suhling JC, Jaeger RC. Silicon piezoresistive stress sensors and their application in electronic packaging. *IEEE Sensors Journal*. 2001;1(1):14-30. https://doi.org/10.1109/JSEN.2001.923584

18. Spencer JL, Schroen WF, Bednarz GA, et al. New quantitative measurements of IC stress introduced by plastic packages. In: Proceedings of the 19th International Reliability Physics Symposium; 1981: 74–80, https://doi.org/10.1109/IRPS.1981.362977.

19. Kanda Y. Piezoresistance effect of silicon. *Sensors and Actuators A*. 1991;28(2):83-91.

20. Becker F, Kuhl M, Manoli Y, Paul O. Novel method to operate piezo-FET-based stress sensor offers tenfold increase in sensitivity. In: Proceedings of the IEEE Sensors 2015; 2015: 1–4. https://doi.org/10.1109/ICSENS.2015.7370482.

21. Doll JC, Pruitt BL. *Piezoresistor Design and Applications*. Springer New York: New York, NY; 2013.

22. King DL, Kratochvil JA, Boyson WE. Temperature coefficients for PV modules and arrays. In: Conference record of the twenty sixth IEEE Photovoltaic Specialists Conference - 1997; 1997: 1183–1186. https://doi.org/10.1109/PVSC.1997.654300.

23. Jeevan Doss CR, Kumaravel M, George B, Jagadeesh Kumar V. An innovative method for determining the junction temperature of a photovoltaic cell. In: IEEE International Instrumentation and Measurement Technology Conference (I2MTC), 2012; 2012: 1847–1850. https://doi.org/10.1109/I2MTC.2012.6229223.

24. Umachandran N, TamizhMani G. Effect of spatial temperature uniformity on outdoor photovoltaic module performance characterization. In: Proceedings of the 43rd IEEE Photovoltaic Specialists Conference (IEEE PVSC); 2016: 2731–2737. https://doi.org/10.1109/PVSC.2016.7750148.

25. Rumble JR. *CRC Handbook of Chemistry and Physics*. 98th ed. Boca Raton, Florida: CRC Press; 2017.